

See discussions, stats, and author profiles for this publication at: <https://www.researchgate.net/publication/338380261>

Automated control algorithms for silicon photonic polarization receiver

Article in *Optics Express* · January 2020

DOI: 10.1364/OE.380121

CITATIONS

8

READS

285

6 authors, including:



Minglei Ma

University of British Columbia - Vancouver

23 PUBLICATIONS 290 CITATIONS

[SEE PROFILE](#)



Hossam Shoman

University of British Columbia - Vancouver

33 PUBLICATIONS 480 CITATIONS

[SEE PROFILE](#)



Lukas Chrostowski

University of British Columbia - Vancouver

345 PUBLICATIONS 7,678 CITATIONS

[SEE PROFILE](#)

Some of the authors of this publication are also working on these related projects:



Bragg grating applications [View project](#)



Broadband Silicon Photonic Optical Add-Drop Filters [View project](#)



Automated control algorithms for silicon photonic polarization receiver

MINGLEI MA, *  HOSSAM SHOMAN,  KEYI TANG, SUDIP SHEKHAR, NICOLAS A. F. JAEGER, AND LUKAS CHROSTOWSKI

Department of Electrical and Computer Engineering, The University of British Columbia, Vancouver, BC Canada V6T 1Z4, Canada

*mingleim@ece.ubc.ca

Abstract: We demonstrate greedy linear descent-based, basic gradient descent-based, two-point step size gradient descent-based, and two-stage optimization method-based automated control algorithms and examine their performance for use with a silicon photonic polarization receiver. With an active feedback loop control process, time-varying arbitrary polarization states from an optical fiber can be automatically adapted and stabilized to the transverse-electric (TE) mode of a single-mode silicon waveguide. Using the proposed control algorithms, we successfully realize automated adaptations for a 10 Gb/s on-off keying signal in the polarization receiver. Based on the large-signal measurement results, the control algorithms are examined and compared with regard to the iteration number and the output response. In addition, we implemented a long-duration experiment to track, adapt, and stabilize arbitrary input polarization states using the two-point step size gradient descent-based and two-stage optimization method-based control algorithms. The experimental results show that these control algorithms enable the polarization receiver to achieve real-time and continuous polarization management.

© 2020 Optical Society of America under the terms of the [OSA Open Access Publishing Agreement](#)

1. Introduction

Silicon photonics has enabled key photonic integrated circuits (PIC) to be realized using CMOS-compatible fabrication. Such silicon PICs offer promising solutions for low-cost, mass-produced, large-scale, integrated-optical interconnects in data centers. Nevertheless, PICs on a silicon-on-insulator (SOI) platform are highly polarization dependent due to the large modal birefringence of SOI waveguides. Particularly, for typical single-polarization, silicon photonic receiver applications, such as wavelength division multiplexing (WDM) receivers, coherent receivers, and multi-channel optical switches, their performance can be detrimentally affected by the polarization mismatch between output of a standard (non-polarization maintaining) optical fiber and the modes of a silicon waveguide. Using polarization maintaining fibres can mitigate the effect, but is an expensive solution to employ in commercial optical systems. In comparison, a cost-effective solution is to use a polarization-transparent PIC, that can be implemented via various techniques.

Polarization diversity [1,2] is a typical approach that simply splits the input light into two branches using a passive photonic integrated device (e.g., a polarization beam splitter (PBS), a polarization splitting grating coupler (PSGC), or a polarization splitter-rotator (PSR)), and implements two identical PICs separately. This method has been recently used and demonstrated in WDM receiver [3–10], coherent receiver [11–14], and optical switch [15] applications. Some photonic integrated devices, such as wavelength add-drop filters [9,10], can be used in a waveguide loop design that is formed between two output ports of a PSR (PBS or PSGC), so that one can re-use the devices. However, many PICs still need to have two identical copies, which is not efficient as regards the required on-chip real estate.

An alternative approach is to develop an active polarization controller [2,16–20]. A PSGC or a PSR is still needed to manage the input polarization states and transmit them into two separate

silicon waveguides. Then, instead of duplicating the PIC, a tunable Mach-Zehnder interferometer (MZI) is connected to the two outputs of the first device (i.e., the PSGC or PSR). The phase shifters in the MZI are used to adjust the phase of the incoming light, such that a desired single polarization can be obtained at one output waveguide of the MZI, and finally pass into the main PIC. Compared to the polarization diversity scheme, this method does not need two copies of the PIC, and, thus, it will reduce the chip area, saving significant footprint and cost, especially for complex PIC designs that require many electrical signals [21–23]. A robust control algorithm is a necessary part of active polarization management. Investigations into the performance of the control algorithms, such as automation, iteration cost of the optimization, and optimization accuracy, are important if one wants to use this approach in real-world optical interconnects. However, although several studies have recently demonstrated active polarization management [17–19], not much effort has been spent on comparing the performance of control algorithms for use in on-chip polarization controllers.

In this paper, we experimentally demonstrate greedy linear descent-based, basic gradient descent-based, two-point step size gradient descent-based, and two-stage optimization method-based control algorithm to automatically adapt an arbitrary input polarization state into the TE mode of, and to continuously stabilize the polarization state in, a single-mode, SOI waveguide of an active polarization receiver (PR). Large-signal measurement results are presented to examine the performance of each studied control algorithm. In addition, by continuously changing the input polarization state, we also implement an experiment to evaluate the stabilization capabilities of the control algorithms used in the PR over a longer duration of time.

2. Design and control algorithms

2.1. PR design and operating principle

A schematic of our polarization receiver is shown in Fig. 1(a). An adiabatic PSR [24] and an MZI form the proposed system. The MZI consists of two thermal phase shifters and two 3-dB adiabatic couplers (ACs) [25] (in fact, all of the components of the PR are adiabatic). Nano-tapered edge couplers are used as the optical I/O ports of the system. The input light, in an arbitrary polarization state, is coupled into the TE and TM modes of the edge coupler and propagates into the PSR. The PSR passively evolves these two modes into the fundamental TE modes of its two output waveguides and then passes them into the balanced MZI. Acting on the outputs of the PSR, the two thermal phase shifters, H1 and H2, control the outputs of the MZI, so that the optical power at the output port is optimized by minimizing the optical power at the feedback port. In this way, an arbitrary input polarization state can be adapted to the fundamental TE mode of the output waveguide. An optical micrograph of a fully fabricated PR is shown in Fig. 1(b).

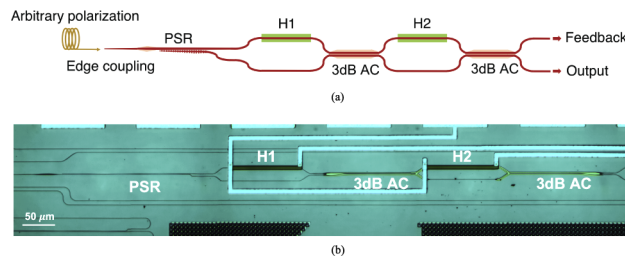


Fig. 1. (a) Schematic of our polarization receiver with an arbitrary polarization input. (b) Optical micrograph of a fabricated polarization receiver.

To confirm our PR's ability to adapt any arbitrary input polarization state to the output TE mode, we experimentally verified the simulations in [18] by tuning the thermal phase shifters, H1

and H2, as shown in Fig. 2. Four input polarization states, resulting in four different TE/TM ratios at the input of the edge coupler, were injected into the PIC. The power distribution of the measured outputs closely matched the simulation results reported in [18]. The distorted regions, such as the "wavy" lower optical power region shown in Fig. 2(a), were mainly attributed to the optical crosstalk in the PSR. The thermal crosstalk in the thermal phase shifters may also cause a shift of the diagrams. In all four cases, maximum power at the output port can be obtained with appropriate control of for H1 and H2, which means that a minimum power was recorded at the feedback port to maximize the output power of the PR. This ability provides a prerequisite to develop an automated control algorithm that can minimize the power at the feedback port. We investigated two types of control algorithm based on two different mathematical optimization methods, which treated the system model of the PR, in one type, as an implicit function, i.e., a "black box," and, in the other type, as a known analytic function.

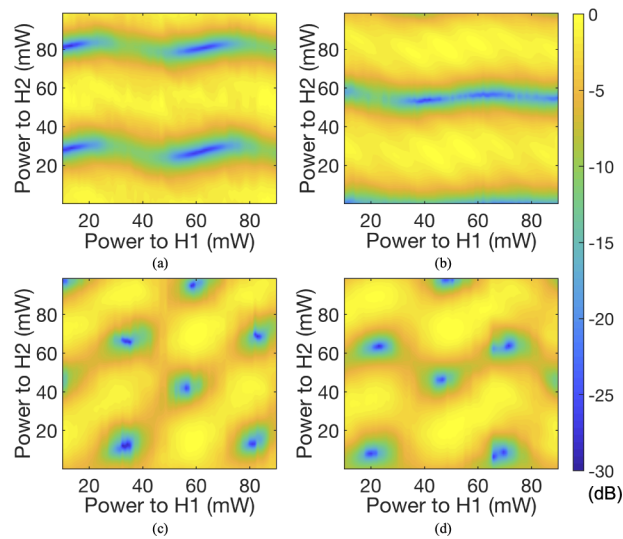


Fig. 2. Measured optical power at the output port with various tuning powers applied to the thermal phase shifters, H1 and H2, for four input polarization ratios: (a) 100% TE mode input, (b) 100% TM mode input, (c) 50% TE and 50% TM mode input, and (d) 75% TE and 25% TM mode input.

2.2. Automated control algorithms

The first type of control algorithm, that treats the entire system as a black box, is generally based on direct minimum search methods. We studied three minimization methods to track the minimum power at the feedback port of the proposed PR: the greedy linear descent (GLD) method, the basic gradient descent (GD) method, and the two-point step size gradient descent (Barzilai and Borwein gradient descent method, B-B GD) method [26]. These methods are illustrated in the flow diagrams shown in Fig. 3. For the GLD method shown in Fig. 3(a), the variables $x_{1,i}$, $x_{2,i}$, and y correspond to currents injected into H1 and H2 and the measured optical power at the feedback port of the PR, respectively. Δp represents the phase tuning step size, that corresponds to the current step being injected into the thermal phase shifters. A closed control loop is used to keep tracking and minimizing the feedback power. The GLD method provides an easy to implement minimum search algorithm for the PR. However, the GLD method's use of a fixed current step size may result in a long convergence time for a small step size, or a failure to converge for a large step size. Therefore, to reduce the iteration number and improve

the robustness of the control algorithm, we used the basic GD method. As shown in Fig. 3(b), instead of a uniform number, the step size of the variable vector \mathbf{x}_i ($\mathbf{x}_i = [x_{1,i}, x_{2,i}]$) is related to a term $\pm \alpha \cdot \mathbf{g}_i$, where the gradient \mathbf{g}_i was re-calculated in each iteration, and the scalar factor α is set to a small real number. Also, a threshold number σ is given to end the control loop when the norm of \mathbf{g}_i decreases to the convergence level. Consequently, given a large initial step size, the basic GD method will be able to locate the minimum feedback power within fewer iterations as compared to the GLD method. However, the constant scalar factor α is still a limitation as regards decreasing the convergence time of the algorithm. Therefore, we employed a known, improved GD method, the B-B GD method [26], in which a new α , α_i , is calculated for each iteration using a two-point approximation to the secant equation underlying quasi-Newton methods. Now, the scalar factor α_i is calculated by

$$\alpha_i = \Delta \mathbf{x}_i \cdot \Delta \mathbf{g}_i^T / \|\Delta \mathbf{g}_i\|^2 \quad (1)$$

where $\Delta \mathbf{x}_i = \mathbf{x}_i - \mathbf{x}_{i-1}$, $\Delta \mathbf{g}_i = \mathbf{g}_i - \mathbf{g}_{i-1}$, and, therefore, the step size, $\pm \alpha_i \cdot \mathbf{g}_i$, would depend on the adjacent points. It has been mathematically proven [26] that the B-B GD method requires less computational effort and is less sensitive to ill-conditioning than the basic GD method, and, thus, the B-B GD-based control algorithm will outperform the basic one. The experimental demonstration on the PR will be presented in Section 3.

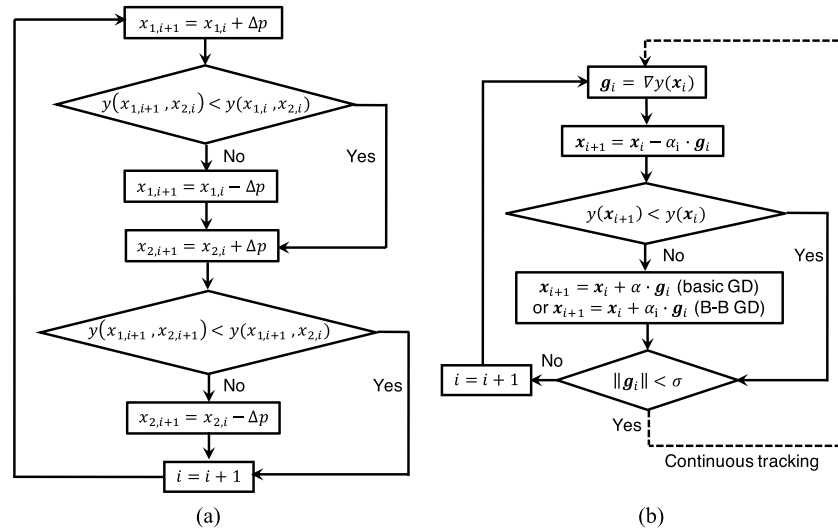


Fig. 3. Flow diagrams illustrating (a) the GLD-based, and (b) the basic GD- and B-B GD-based minimization method for the control algorithms.

The second type of control algorithm is a single-iteration, two-stage method based on mathematical optimization functions. As shown in Fig. 4(a), a four-step workflow - initializing, sampling, training, and minimizing ("ISTM") forms the first stage of the control process. As we mentioned previously, a known, systematic, analytic function, $f(\mathbf{x}, h_1, h_2)$, is needed and given by

$$f(\mathbf{x}, h_1, h_2) = E_1(\mathbf{x}, h_1, h_2), \quad (2)$$

$$E_{\text{out}}(\mathbf{x}, h_1, h_2) = \begin{bmatrix} E_1(\mathbf{x}, h_1, h_2) \\ E_2(\mathbf{x}, h_1, h_2) \end{bmatrix} = M(\mathbf{x}) \cdot E_{\text{in}}(h_1, h_2) \quad (3)$$

where the 2×2 matrix, M , and the 2×1 matrix, E_{in} , correspond to the theoretical model and the inputs of the MZI, i.e., the outputs of the PSR, respectively. Using the transfer matrix

method [27], the 2×1 output matrix of the MZI, E_{out} , is derived using Eq. 3. The vector \mathbf{x} still corresponds to the currents injected into H1 and H2, and there are two "hidden" parameters, h_1 and h_2 , which are related to the power percentage in one input of the MZI and the phase difference between the two inputs of the MZI, respectively. Except for h_1 and h_2 , all of the other parameters in $f(\mathbf{x}, h_1, h_2)$ were obtained using the design parameters and the simulation results for the PR (e.g., S-parameter matrices for the ACs). In addition, it should be mentioned that an experimental curve fitting correlation between the phase shift and the current injections was also made (see Appendix), which relates the phase change in the analytic function to the injected currents into H1 and H2.

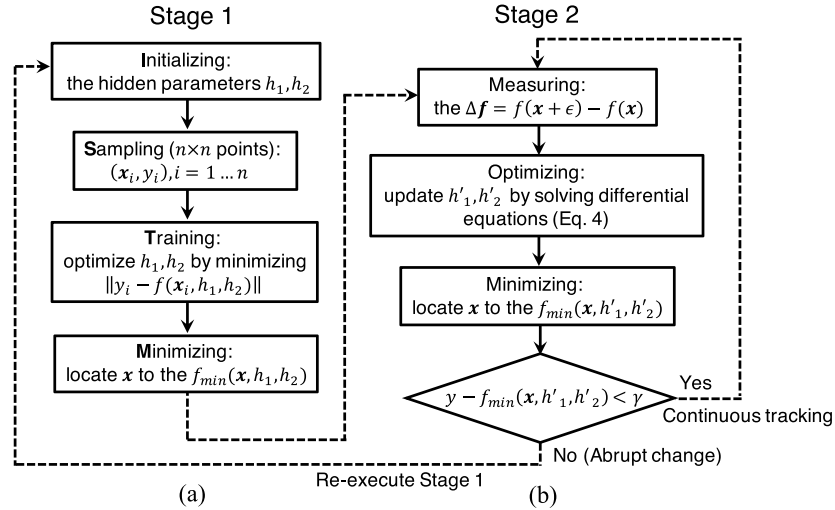


Fig. 4. Flow diagram illustrating the minimization process for the single-iteration, two-stage control algorithm: (a) an "ISTM" method for Stage 1 and (b) a dynamic minimum tracking method for Stage 2.

Hence, in order to automatically locate a minimum power at the feedback port of the PR, the control algorithm was started by following the "ISTM" steps in Stage 1 (in Fig. 4(a)). To begin with, two initial numbers for h_1 and h_2 were given to the analytic function $f(\mathbf{x}, h_1, h_2)$. Next, a group of sample points (x_i, y_i) , where y_i is the sampled optical power at the feedback port, were chosen and measured as a preparation for the following optimization process. Then, for the training step, we defined and minimized the amplitude of the "residual" function $\|y_i - f(x_i, h_1, h_2)\|$, such that h_1 and h_2 could be trained simultaneously and finally optimized. Here, a non-linear least-squares solver [28] was employed to realize a rapid optimization process. Lastly, with the optimized h_1 and h_2 , one of the minimum points for $f(\mathbf{x}, h_1, h_2)$ could be quickly located using the Newton-Conjugate-Gradient (Newton-CG) method [29], which told us the currents that should be injected into H1 and H2 in order to obtain the minimum optical power at the feedback port.

However, as the input polarization state may vary continuously, h_1 and h_2 can drift overtime. Thus, in Stage 2, a dynamic tracking method is needed to keep updating the function parameters (h_1 and h_2) without repeating the sampling step. As shown in Fig. 4(b), firstly, output differences, Δf , were measured by adding a perturbation ϵ to the variable vector \mathbf{x} . Then, the instantaneous h'_1 and h'_2 were determined by the following differential equation:

$$\Delta f = \frac{\partial f(\mathbf{x}, h'_1, h'_2)}{\partial \mathbf{x}} \cdot \epsilon \quad (4)$$

where $\frac{\partial f(x, h'_1, h'_2)}{\partial x}$ is the partial derivative of the analytic function. Using the Newton-Raphson method [30], we could solve the equations numerically to obtain h'_1 and h'_2 . Finally, with the updated parameters, we adjusted the currents injected into H1 and H2 to maintain the minimum power at feedback port. Here, it should be noted that, if some abrupt change occurs (e.g., a discontinuous change of the polarization state or a major optical power fluctuation) during the tracking process, i.e., the measured optical power at the feedback port (y in Fig. 4(b)) is significantly larger than the minimum optical power at feedback port ($f_{\min}(x, h'_1, h'_2)$ in Fig. 4(b)), Stage 1 needs to be re-executed to update the analytic function. A threshold γ needs to be given to determine whether re-executing Stage 1, as shown in Fig. 4(b).

Benefiting from the use of the analytic function, the two-stage control algorithm has several advantages as compared with the first type of control algorithms i.e., the GLD, basic GD, and B-B GD method. In Stage 1, the more sampling points we have, the higher measurement tolerance the system model will have. This provides us with more flexibility to efficiently adjust the accuracy based on the measurement tolerances such as optical alignment errors, fluctuations of the output power, and noise level of the optical feedback power. In Stage 2, the output response of the PR can be stabilized by introducing only a small perturbation. However, any of the first type control algorithms can be used in Stage 2. In addition, it should be noted that some experimental factors, such as thermal drift and power fluctuations, may effect the tracking results.

3. Experiments and results

The test structures were fabricated using 193 nm optical lithography at the Institute of Micro-electronics (IME), Singapore. As shown in Fig. 6, a high-speed experimental setup was built to test the performance of the fabricated PRs using the control algorithms. A non-return-to-zero (NRZ) $2^{31} - 1$ pseudorandom binary sequence (PRBS) data stream, provided by a pulse pattern generator (PPG), was applied to a LiNbO₃ Mach-Zehnder modulator (MZM) to generate 10 Gbps modulated optical signals. An off-chip polarization controller (PC) was then used to generate the arbitrary polarization states injected into the PR, and, in order to monitor these polarization states in the optical fiber, we used a 10/90 polarization-maintaining fiber-optic tap to couple 10 percent of the transmitted light into a polarization extinction ratio meter (PEM). Here, it should be noted that, although we used polarization-maintaining (PM) fiber throughout our measurement setup, other than the fiber in the PC, the polarization states that we obtained from the PEM are, in general, different from the polarization states injected into the chip. However, the two orthogonal s and p polarizations will be maintained by the PM fiber and only the phase difference between them will change. Therefore, when only one of these two polarization states (s and p) is measured by the PEM, we know that it is the polarization state injected into our chip; the orthogonal states shown in Fig. 5(c) represent the s and p polarization states with ~ 15 dB polarization extinction ratios. The other polarization states recorded in Fig. 5(c) provide evidence that a range of arbitrary polarization states were injected into our PR. For the on-chip control process, a current source meter and an external photodetector (PD) were employed to tune the thermal phase shifters and read the optical power at the feedback port of the PR. The output light was detected by a high-speed photoreceiver (Rx), and an erbium-doped fiber amplifier (EDFA) and a variable optical attenuator (VOA) were placed ahead of the Rx to set a desirable optical power level. The detected RF output was finally sent to an oscilloscope for the eye diagram measurement and an error detector (ED) for the bit-error ratio (BER) measurement.

Figure 6 shows the measured BERs and optical powers for each of the control algorithms applied to the DUT. An arbitrary polarization state that would result in a high optical power at the feedback port, i.e., a low optical power and high BER measured at the output port, was launched into the PR. This initial input case can be considered as an abrupt change of the polarization state in an optical fiber. Then, we implemented the control algorithms. As shown in Fig. 6, by implementing the B-B GD-based, basic GD-based, GLD-based, or ISTM-based control

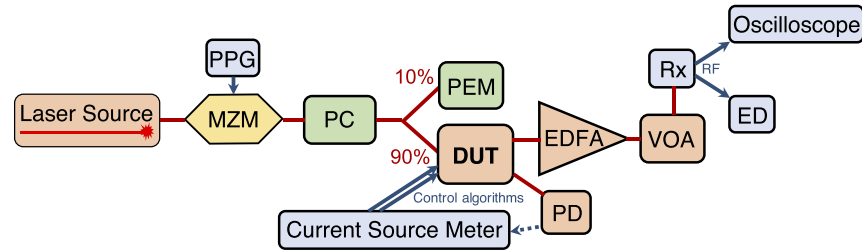


Fig. 5. Schematic of the experimental setup for eye diagram and BER measurements.

algorithm, the optical power at the feedback port was minimized to obtain at least a ~ 30 dB power extinction ratio relative to the power at the output port, and correspondingly low BERs (10^{-9} – 10^{-10}) at the output port. Here, we should also note that fluctuations of the optimized BER data were mainly due to a short averaging time (1s) of the ED and minor changes in the optical coupling. More importantly, based on the BERs in Fig. 6(a), we can also see a significant difference in the number of iterations that were needed to accomplish the optimization process: 19 iterations for the GLD method, 6 iterations for the basic GD method, 3 iterations for the B-B GD method, and 1 iteration for the ISTM method. These measurement results indicate that, for

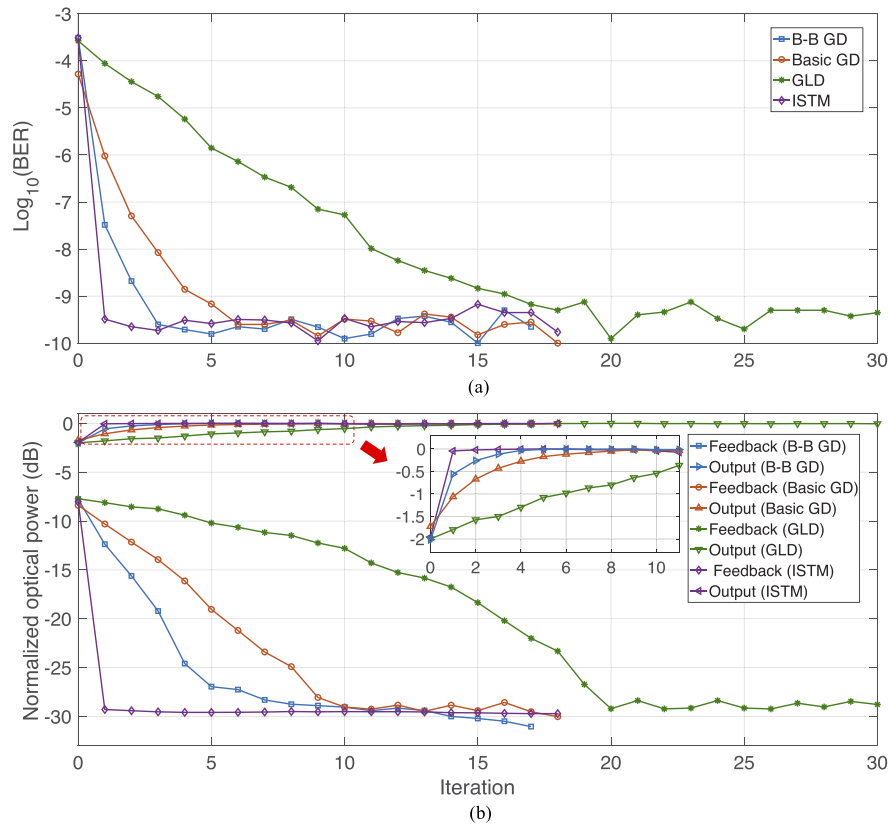


Fig. 6. Measurement results for four control algorithms: (a) BERs versus iteration and (b) normalized optical power at the output power and feedback ports of the PR versus iteration. Inset Fig.: Zoom-in of the measured optical power at the output port.

an arbitrary input polarization state, all of the automated control algorithms accomplish a similar level of optimized accuracy, i.e., they can adapt the input into a desired, optimized TE output mode, while the B-B GD-based and the ISTM-based control algorithms take fewer iterations to obtain the optimized output.

In addition, due to the polarization-dependent loss (PDL), mainly coming from the edge couplers and PSR, the optimized optical output power would vary with different input polarization state, even for constant input powers. Thus, we also measured BERs and eye diagrams versus the input power for four polarization states (Pol. state 1 - 4 in Fig. 7). As shown in Fig. 7(a), by changing the polarization angle of the polarization state in the fiber, i.e., rotating a slow-axis polarization state ("TE-like" polarized mode) to a fast-axis polarization state ("TM-like" polarized mode) coupled into our input waveguide, larger BERs were obtained. This increase in BER was due to higher losses for the TM-like mode. On the other hand, based on the curve-fittings (Pol. state 1 and 4), we could also estimate ~ 1.5 dB PDL in our test PR. The PDL impact is reflected by the amplitude decrease of the eyes when changing from TE- to TM-like polarized modes. This was also observed for various input power levels, see Fig. 7(b).

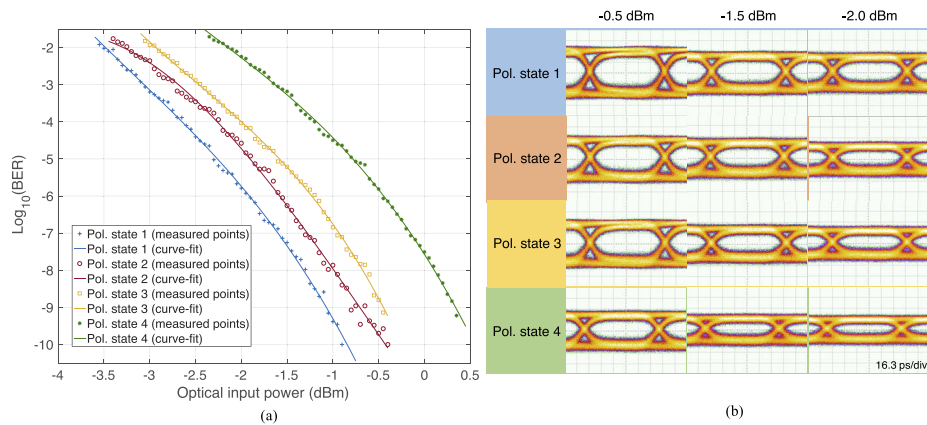


Fig. 7. (a) BER versus optical input power (markers for measured BERs and solid lines for the polynomial fittings) and (b) some measured eye diagrams with four different polarization states in the optical fiber. The polarization angles of the polarization state 1 - 4: 3.0 degree, 13.5 degree, 22.8 degree, and 84.6 degree.

Furthermore, we implemented a tracking and stabilization test by continuously changing the input polarization states using the external PC. As shown in Fig. 8, the test PR optimized and stabilized the arbitrary input polarization states using both the B-B GD-based and two-stage control algorithm. In Fig. 8(c), the polarization angles and extinction ratios, monitored by the PEM, provided the angle of the major axes and ellipticities of the polarizations measured. As we mentioned previously, for the s and p polarizations on their own, it can also indicate the power launched into either the TE-like mode or the TM-like mode of the on-chip waveguide. The BER and the optical power at the feedback port are presented in Figs. 8(a) and 8(b). As a reference, the output responses without any control algorithm were also measured.

We can see that the feedback power was constantly minimized and stabilized by using both the B-B GD-based and two-stage control algorithm, and, thus, the BER stayed at a lower level as compared to the response without any control. However, it should be noted that, due to the PDL impact mentioned previously, the optimized BER for both methods exhibited a higher level ($10^{-6} \sim 10^{-8}$) when the light injected into our PR was primarily in the TM-like modes. We can reduce this PDL impact by compensating the optical input power.

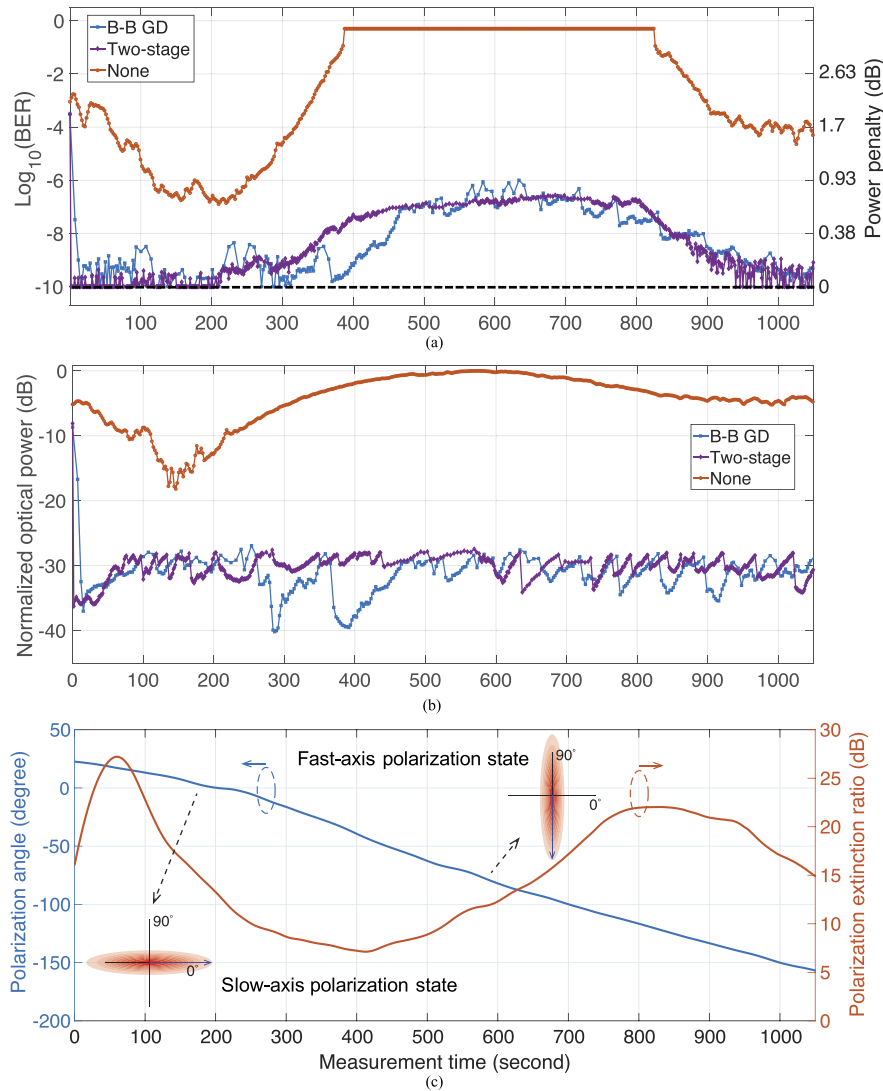


Fig. 8. Measurement results of tracking and stabilization of continuous changed input polarization states: (a) BERs versus tracking time, a reference BER level (dash line), and optical power penalty to achieve a BER of 10^{-10} ; (b) Normalized optical power at feedback port of the PR versus tracking time; (c) Polarization angles and extinction ratios of the transmitted light in the optical fiber versus tracking time, and electric field distributions of slow-axis and fast-axis polarization state.

While the paper is focused on our automated control algorithms, it is worth discussing the active polarization receiver that we used. First, the electric powers that need to be applied to the phase shifters of the MZI depend on the input polarization state. Given that the input polarization state is also wavelength dependent, this leads to the electric power that needs to be applied to the phase shifters also being wavelength-dependent. Also, adapting a particular polarization state to the TE-like output mode requires cancelling the group delay difference between the outputs of the PSR. It has been suggested that implementing a variable optical delay line after one of the outputs of PSR can be used to compensate for such group delay difference [16,22]. Second, the

polarization receiver used here is not an endless polarization tracking design [21,22]. Additional MZIs are required to implement such endless tracking. Nevertheless, the automated control algorithms demonstrated in the paper can easily be adapted to be used with any polarization receiver design.

4. Conclusion

In summary, we have experimentally demonstrated greedy linear descent-based, basic gradient descent-based, two-point step size gradient descent-based, and two-stage optimization method-based automated control algorithms for use with an active polarization receiver. High-speed, large-signal measurements, for all of the control algorithms, show similar output responses after the automated control, while different iterations are needed for the various control process to converge. The PDL impact on the large-signal outputs has also been verified and discussed. Furthermore, using the two-point step size gradient descent-based and the two-stage optimization method-based control algorithm, we have presented long-duration, large-signal measurements. The results indicate that these two control algorithms can enable the polarization receiver to continuously adapt and stabilize the arbitrary polarization states, which change from a standard optical fiber, into the TE-like mode of our output waveguide. The demonstrated automated control algorithms can also be used for WDM-polarization applications. An expanded polarization receiver, which combines wavelength de-multiplexers to separate the input signal into individual transmitted wavelength-channels, each with its own polarization receiver, would be required.

Appendix: Phase shift - current relation derivation

For the phase shifters, a phase shift $\Delta\varphi$ is normally realized by introducing an effective index change Δn_{eff} in the waveguide and is given by

$$\Delta\varphi = \frac{2\pi L}{\lambda_0} \Delta n_{\text{eff}} \quad (5)$$

where L is the length of the waveguide, λ_0 is the operating wavelength. As we use thermal phase shifters, Δn_{eff} can be correlated to the temperature variation ΔT in the waveguide by

$$\Delta n_{\text{eff}} = \frac{dn_{\text{eff}}}{dT} \Delta T \quad (6)$$

where $\frac{dn_{\text{eff}}}{dT}$ depends on the waveguide material. Also, to determine the energy ΔQ consumed by the thermal phase shifters that corresponds temperature change ΔT in the waveguide, we use the heat transfer formula,

$$\Delta Q = mc_h \Delta T \quad (7)$$

where m is the mass and c_h is the specific heat of the material. Overall, based on Eqs. 6 and 7, we can derive the injected energy per unit time, i.e., the electric power P , as follows:

$$P = \Delta Q = mc_h \Delta T = mc_h \frac{\Delta n_{\text{eff}}}{\frac{dn_{\text{eff}}}{dT}} = \frac{mc_h \lambda}{\frac{dn_{\text{eff}}}{dT} 2\pi L} \Delta\varphi \quad (8)$$

Therefore, a linear relation between the phase shift and the applied electric power is obtained. Then, to determine $\Delta\varphi$ as a function of injected current, we need to measure one of the output spectra of a 2×2 MZI with a TE input mode, and implement a curve-fit to the measured spectrum

using following equation:

$$P_{\text{out}} = 0.5 \cdot (1 + \cos(\Delta\varphi)) \quad (9)$$

where P_{out} is the optical output power of the MZI. Since we know the relation in Eq. 8, the phase shift $\Delta\varphi$ can be replaced by

$$\Delta\varphi = \alpha P + \beta = \alpha(I^2 R) + \beta \quad (10)$$

where R is the resistance of thermal phase shifter, I is the injected current, and α and β are determined by the curve-fit. Finally, the relation between the phase shift $\Delta\varphi$ and the injected current I is achieved.

Funding

Natural Sciences and Engineering Research Council of Canada.

Acknowledgements

We acknowledge CMC Microsystems for the design software and providing access to the fabrication. We also thank Dr. Dylan Logan and Dr. Edgar Huante Ceron at Ranovus Inc. for helpful discussions.

Disclosures

The authors declare no conflicts of interest.

References

1. T. Barwicz, M. R. Watts, M. A. Popović, P. T. Rakich, L. Socci, F. X. Kärtner, E. P. Ippen, and H. I. Smith, "Polarization-transparent microphotonic devices in the strong confinement limit," *Nat. Photonics* **1**(1), 57–60 (2007).
2. L. Chrostowski and M. Hochberg, *Silicon photonics design: from devices to systems* (Cambridge University, 2015).
3. L. Chen, C. R. Doerr, and Y.-K. Chen, "Polarization-diversified DWDM receiver on silicon free of polarization-dependent wavelength shift," in *Optical Fiber Communication Conference*, (IEEE, 2012), pp. 1–3.
4. P. De Heyn, J. De Coster, P. Verheyen, G. Lepage, M. Pantouvaki, P. Absil, W. Bogaerts, D. Van Thourhout, and J. Van Campenhout, "Polarization-insensitive 5×20Gb/s WDM Ge receiver using compact Si ring filters with collective thermal tuning," in *Optical Fiber Communication Conference*, (Optical Society of America, 2014), pp. Th4C–5.
5. P. Dong, Y.-K. Chen, and L. L. Buhl, "Reconfigurable four-channel polarization diversity silicon photonic WDM receiver," in *Optical Fiber Communication Conference*, (Optical Society of America, 2015), pp. W3A–2.
6. Y. Ma, Y. Liu, H. Guan, A. Gazman, Q. Li, R. Ding, Y. Li, K. Bergman, T. Baehr-Jones, and M. Hochberg, "Symmetrical polarization splitter/rotator design and application in a polarization insensitive WDM receiver," *Opt. Express* **23**(12), 16052–16062 (2015).
7. D. Y. Lee, X. Zheng, J. Yao, Y. Luo, J.-H. Lee, S. Lin, H. Thacker, J. Bovington, I. Shubin, S. S. Djordjevic, J. E. Cunningham, K. Raj, and A. V. Krishnamoorthy, "Error-free operation of a polarization-insensitive 4λ × 25 Gbps silicon photonic wdm receiver with closed-loop thermal stabilization of Si microrings," *Opt. Express* **24**(12), 13204–13209 (2016).
8. R. Gatdula, K. Kim, A. Melikyan, Y.-K. Chen, and P. Dong, "Simultaneous four-channel thermal adaptation of polarization insensitive silicon photonics WDM receiver," *Opt. Express* **25**(22), 27119–27126 (2017).
9. Y. Tan, H. Wu, and D. Dai, "Silicon-based hybrid (de) multiplexer for wavelength-/polarization-division-multiplexing," *J. Lightwave Technol.* **36**(11), 2051–2058 (2018).
10. A. H. K. Park, H. Shoman, M. Ma, S. Shekhar, and L. Chrostowski, "Ring resonator based polarization diversity WDM receiver," *Opt. Express* **27**(5), 6147–6157 (2019).
11. C. R. Doerr, P. J. Winzer, Y.-K. Chen, S. Chandrasekhar, M. S. Rasras, L. Chen, T.-Y. Liow, K.-W. Ang, and G.-Q. Lo, "Monolithic polarization and phase diversity coherent receiver in silicon," *J. Lightwave Technol.* **28**(4), 520–525 (2010).
12. A. H. Ahmed, D. Lim, A. Elmoznine, Y. Ma, T. Huynh, C. Williams, L. Vera, Y. Liu, R. Shi, M. Streshinsky, A. Novack, R. Ding, R. Younce, J. Roman, M. Hochberg, S. Shekhar, and A. Rylyakov, "30.6 A 6V Swing 3.6% THD > 40GHz Driver with 4.5× Bandwidth Extension for a 272Gb/s Dual-Polarization 16-QAM Silicon Photonic Transmitter," in *2019 IEEE International Solid-State Circuits Conference (ISSCC)*, (IEEE, 2019), pp. 484–486.
13. A. Melikyan, K. Kim, N. Fontaine, S. Chandrasekhar, Y.-K. Chen, and P. Dong, "Inter-polarization mixers for coherent detection of optical signals," *Opt. Express* **26**(14), 18523–18531 (2018).
14. A. Melikyan, N. Kaneda, K. Kim, and P. Dong, "Inter-polarization 180-degree mixer for reception of m-ask signals," in *2018 European Conference on Optical Communication (ECOC)*, (IEEE, 2018), pp. 1–3.

15. S.-H. Kim, K. Tanizawa, Y. Shoji, G. Cong, K. Suzuki, K. Ikeda, H. Ishikawa, S. Namiki, and H. Kawashima, "Compact 2×2 polarization-diversity Si-wire switch," *Opt. Express* **22**(24), 29818–29826 (2014).
16. W. D. Sacher, T. Barwicz, B. J. Taylor, and J. K. Poon, "Polarization rotator-splitters in standard active silicon photonics platforms," *Opt. Express* **22**(4), 3777–3786 (2014).
17. J. N. Caspers, Y. Wang, L. Chrostowski, and M. Mojahedi, "Active polarization independent coupling to silicon photonics circuit," in *Silicon Photonics and Photonic Integrated Circuits IV*, vol. 9133 (International Society for Optics and Photonics, 2014), p. 91330G.
18. M. Ma, K. Murray, M. Ye, S. Lin, Y. Wang, Z. Lu, H. Yun, R. Hu, N. A. F. Jaeger, and L. Chrostowski, "Silicon photonic polarization receiver with automated stabilization for arbitrary input polarizations," in *CLEO: Science and Innovations*, (Optical Society of America, 2016), pp. STu4G–8.
19. P. Velha, V. Sorianello, M. Preite, G. De Angelis, T. Cassese, A. Bianchi, F. Testa, and M. Romagnoli, "Wide-band polarization controller for Si photonic integrated circuits," *Opt. Lett.* **41**(24), 5656–5659 (2016).
20. H. Zhou, Y. Zhao, Y. Wei, F. Li, J. Dong, and X. Zhang, "All-in-one silicon photonic polarization processor," *Nanophotonics* **8**(12), 2257–2267 (2019).
21. C. R. Doerr and L. Chen, "Monolithic PDM-DQPSK receiver in silicon," in *36th European Conference and Exhibition on Optical Communication*, (IEEE, 2010), pp. 1–3.
22. C. R. Doerr, N. K. Fontaine, and L. L. Buhl, "PDM-DQPSK silicon receiver with integrated monitor and minimum number of controls," *IEEE Photonics Technol. Lett.* **24**(8), 697–699 (2012).
23. D. A. B. Miller, "Self-configuring universal linear optical component," *Photonics Res.* **1**(1), 1–15 (2013).
24. M. Ma, A. H. Park, Y. Wang, H. Shoman, F. Zhang, N. A. F. Jaeger, and L. Chrostowski, "Sub-wavelength grating-assisted polarization splitter-rotators for silicon-on-insulator platforms," *Opt. Express* **27**(13), 17581–17591 (2019).
25. H. Yun, W. Shi, Y. Wang, L. Chrostowski, and N. A. F. Jaeger, "2×2 adiabatic 3-dB coupler on silicon-on-insulator rib waveguides," in *Photonics North 2013*, vol. 8915 (International Society for Optics and Photonics, 2013), p. 89150V.
26. J. Barzilai and J. M. Borwein, "Two-point step size gradient methods," *IMA J. Numer. Analysis* **8**(1), 141–148 (1988).
27. C. K. Madsen and J. H. Zhao, *Optical filter design and analysis* (Wiley, 1999).
28. SciPy community, "Solve a nonlinear least-squares problem with bounds on the variables," https://docs.scipy.org/doc/scipy/reference/generated/scipy.optimize.least_squares.html.
29. R. Fletcher and C. M. Reeves, "Function minimization by conjugate gradients," *The Comput. J.* **7**(2), 149–154 (1964).
30. A. Ben-Israel, "A Newton-Raphson method for the solution of systems of equations," *J. Math. Analysis Appl.* **15**(2), 243–252 (1966).